

MATHEMATICAL MODELING OF COLLECTIVE CELL MIGRATION

BSC THESIS APPLIED MATHEMATICS

LEONARD STEVENS - 5806380

Supervisors

Dr. E. G. Rens

Dr. Q. Peng (Lancaster University & Leiden University)

Committee members

Dr. J.L.A. Dubbeldam

Dr. N. V. Budko

JUNE, 2025



Abstract

Collective cell migration is an important activity during the process of wound healing. In this thesis, we develop a model of a wound-healing assay using the Cellular Potts Model in the software package Morpheus. In addition, we describe a system of three coupled partial differential equations for different forms of the molecule transforming growth factor β . An analysis of this system shows the existence of a trivial and an infeasible homogeneous steady state solution, but the system does not allow Turing patterns to form. A baseline migration model with circular-shaped fibroblast cells is set up and tested. This model is extended by modeling the elongated shape of fibroblasts, which showed an increased amount of vertical cell movement. An in-depth analysis is performed to investigate the effect of cell length on vertical cell movement. It shows a significant increase in vertical movement when increasing the cell length up to approximately a factor of 2. Lastly, as a proof of concept, the reaction-diffusion system is integrated into the extended model simulating the differentiation of fibroblasts into myofibroblasts.

Contents

1	Introduction	3
1.1	Wound Healing	3
1.2	Using Mathematical Modeling	5
1.3	Thesis Outline	5
2	The Cellular Potts Model	6
2.1	Representing a cell	6
2.2	The Hamiltonian	8
2.3	Model Assumptions	10
3	The Reaction-Diffusion Model	11
3.1	Model Description	11
3.2	Turing Pattern Analysis	12
3.2.1	Homogeneous Steady State Solutions	13
3.2.2	Stability of Homogeneous Steady State Solutions	14
3.2.3	Non-Existence of Wave-number	14
3.3	Numerical Analysis	14
4	Wound-Healing Assay Simulations	17
4.1	Baseline model	17
4.2	Baseline Model with Additional Shape Constraints	19
4.2.1	The Effect of Cell Length on Vertical Movement	21
4.3	Proof of Concept Model with Differentiation	23
5	Conclusion and Discussion	25

1 Introduction

1.1 Wound Healing

Wound healing is a process that is critical to maintaining human life. It is a complex process that involves many factors. In this section, we will go over the basic principles of the complete wound healing process, after which we will dive further into the specifics of cell migration and the properties of transforming growth factor β (TGF- β).

In the process of wound healing, there are a number of different cells that play important roles. We will first look at the three most important cells, these are macrophages, fibroblasts and myofibroblasts. Macrophages are a type of white blood cell and are responsible for killing and cleaning up pathogens and other foreign substances. Fibroblasts and myofibroblasts are cells that contribute to wound healing by producing a protein called collagen, which is essential for repairing damaged skin and provides strength and integrity. These two cells are somewhat similar but most notably differ in shape, fibroblasts are elongated and myofibroblasts are more star-shaped, see Figure 1.1.

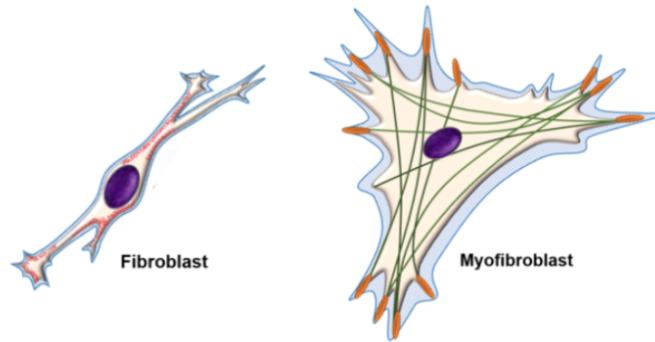


Figure 1.1: Illustration of a fibroblast and a myofibroblast [1].

Wound healing can be split up into four distinct but partially overlapping stages: hemostasis, inflammation, proliferation and remodeling. Hemostasis is the first stage and is characterized by bleeding and the formation of a blood clot. The platelets present in this clot also release a number of proteins called growth factors, among these proteins are platelet-derived growth factor (PDGF) and TGF- β . These growth factors attract and activate macrophages and fibroblasts.

During the inflammation stage, bacteria are killed and disposed of and epithelial cells start to form a basement membrane covering the wound area. The newly arrived macrophages further clean up the wound and start producing growth factors, including TGF- β .

Fibroblasts migrate towards the wound area as a result of the growth factors released by the macrophages and PDGF, which marks the start of the proliferation

stage. These fibroblasts then produce collagen for the production of a new extracellular matrix (ECM) which provides structural support and is a crucial basis for cell migration. Additionally, granulation tissue forms, new blood vessels are created and epithelialization occurs. During the latter process a single layer of epidermal cells covers the wound area by migrating from the wound edges. The final stage of wound healing is called remodeling and is characterized by a continuous process of breaking down and reforming collagen bundles. This final stage can take weeks or even months [2].

This project focuses mainly on the proliferation stage, in particular the collective migration of cells. We will use a computational model of a wound-healing assay (or scratch assay). This is an experimental method where a monolayer of cells is grown *in vitro* such that the layer uniformly covers an area. Then, a scratch is made in the monolayer, creating a region that is devoid of cells. The cells then start to migrate to close the gap. This method allows us to study cell migration as a collective instead of just as a single cell, this more closely resembles actual wound healing.

Cell migration can, in certain situations, be caused by a concentration gradient of some substance. This process of cell migration up a concentration gradient is called chemotaxis. Early research suggests that TGF- β is the main chemo-attractant for fibroblast migration [3]. There are, however, not many sources supporting this claim and the research originates from some decades ago (1987). In this project, we will use a general polarization model for cell migration that is not linked with TGF- β . During collective migration, cells obtain front-rear polarity and through a number of biochemical processes the cells start to migrate in the direction of the polarization [4]. This polarization is initiated at the leading edge of the cells and slowly propagates backward. However, it is not yet well understood how this polarization synchronizes across all cells [5]. Although, research did show that persistent cell movement reinforces cell polarity, creating a loop between cell movement and polarity [6].

During the proliferation stage, fibroblasts can differentiate into myofibroblasts under the influence of TGF- β [7]. This differentiation can only occur when TGF- β is in its active and freely diffusing form. After secretion of TGF- β by the wound, it forms a structure called the large latent complex (LLC). This LLC can freely diffuse, but the TGF- β within it is in a deactivated state. LLC can bind to receptors in the ECM. Subsequently, the TGF- β can be freed and activated, see Figure 1.2.

In addition to having a different shape from fibroblasts, myofibroblasts are also more motile and contract more. This higher contractile activity has been shown to stimulate TGF- β activation.

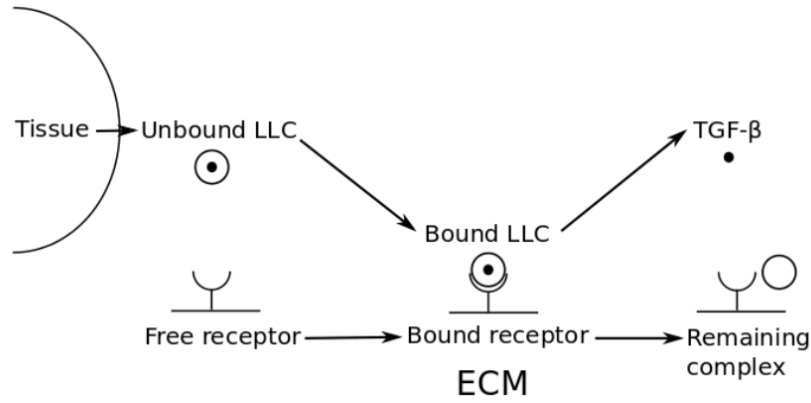


Figure 1.2: Illustration of the different forms of TGF- β .

1.2 Using Mathematical Modeling

In this project we use mathematical modeling to increase our understanding of the biological process of collective migration in wound healing. However, it is important to note that a mathematical model is a simplified representation and does not capture all aspects of the biological system. We make use of a model as some phenomena are difficult to study experimentally. Once the model represents reality well enough, we may expand it to come up with new hypotheses.

Mathematical models, however, do introduce certain challenges. For example, it can also be difficult to know when the model is realistic, as not all results can be empirically verified. A lot of the model parameters are also unknown or do not translate well into reality. For this reason, we must approximate many parameters by trial and error to acquire realistic results. Additionally, almost all of the parameter values used in this project are either dimensionless or do not have an actual scientific unit. We are interested in studying the behavior of the migrating cells and for this reason, we will not go into the units.

1.3 Thesis Outline

This project focuses on the mathematical modeling of collective cell migration. We study this process using a wound-healing assay setup and model the cell migration using the Cellular Potts Model (CPM), which is described in Section 2. We combine this model with a system of coupled partial differential equations for an important growth factor protein called transforming growth factor- β (TGF- β). In Section 3 we describe this system of equations and perform analytical and numerical analyses on it. Then, in Section 4 we combine the system of equations into the CPM and we view the results of different model simulations and test the effects of varying cell shapes. Finally, the conclusion and discussion are found in Section 5.

2 The Cellular Potts Model

In order to analyze cell migration in the process of wound healing, we use a discrete mathematical model called the Cellular Potts Model (CPM), a commonly used agent-based mathematical model for simulating cell behavior. This CPM is an adaptation of the Potts model which in turn is a generalization of the Ising model, which is used in statistical mechanics to simulate magnetic fields. We will implement the Cellular Potts Model using a software program named Morpheus [8]. In the following subsections, we explain the CPM.

2.1 Representing a cell

In the CPM each cell is represented as a finite collection of pixels in a two- or three-dimensional grid, but for this project we will only consider the two-dimensional case. Each cell is assigned a spin value $\sigma \in S = \{1, 2, 3, \dots, n\}$ where n is the number of cells. Let $\tau : S \rightarrow T$ be the function from the set of spins S to the set of cell types T that assigns to each spin value σ its corresponding cell type $\tau(\sigma)$. In this model the fibroblasts are assigned cell type $\tau(\sigma) = 1$ and the myofibroblasts are assigned to $\tau(\sigma) = 2$. Typically, one uses $\tau(\sigma) = 0$ to represent the medium surrounding the cells, which is usually the ECM. Figure 2.1 shows a typical schematic of the domain of the CPM: yellow, red and blue are three different cells, and white pixels are the medium.

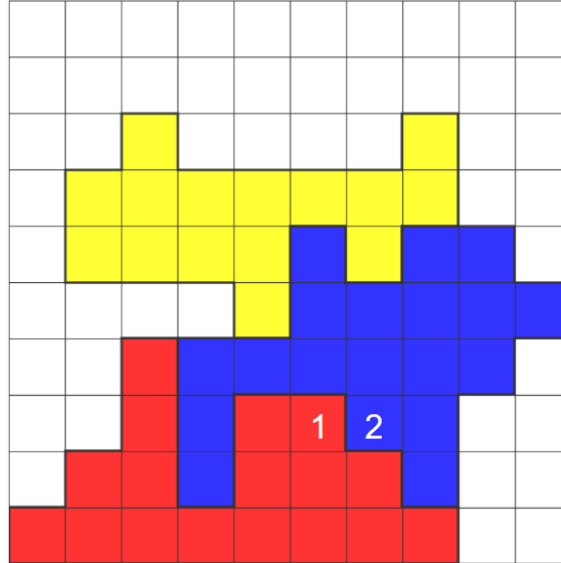


Figure 2.1: Representation of three different cells and surrounding medium on a 10 by 10 grid. Sites 1 and 2 are highlighted for use in the example below.

These cells can evolve and change shape over time. First, an initial configuration is created. Then, at each timestep, called a Monte Carlo step, the model can impose certain adjustments to the shape of the cells. Before executing these alterations, the Hamiltonian (\mathcal{H}) representing the total amount of energy of the system is taken into account. If the Hamiltonian decreases when applying the change ($\Delta\mathcal{H} \leq 0$), it is accepted. However, if the Hamiltonian increases when applying the change

($\Delta\mathcal{H} > 0$), the alteration is accepted with a small probability which depends on $\Delta\mathcal{H}$. One might think that energetically unfavorable ($\Delta\mathcal{H} > 0$) adjustments should always be rejected. When this is the case, however, the cell configuration may move towards a local equilibrium and eventually stop moving. An aspect of random sporadic movement is also included in the model. This inclusion of random movement makes the model more realistic, real biological cells also possess this behavior and it also makes the cells able to escape local minima.

Below we describe the Monte Carlo algorithm for updating the model. Take Figure 2.1 as an example. The algorithm selects one grid site at random and one of its neighboring sites at random. We define two grid sites to be neighbors when they either share a corner or an edge, so each grid site which is not at the boundary has eight neighbors. Suppose the algorithm happens to select site 1 and site 2 as its neighbor. It then makes an attempt at copying the spin of site 1 into site 2, see Figure 2.2 for the updated configuration. It will calculate the Hamiltonian before and after the potential spin copy, giving us a value for $\Delta\mathcal{H}$. The potential spin copy is now accepted with probability

$$\mathcal{P}(\Delta\mathcal{H}) = \begin{cases} \exp\left(\frac{-\Delta\mathcal{H}}{T}\right), & \text{if } \Delta\mathcal{H} > 0 \\ 1, & \text{if } \Delta\mathcal{H} \leq 0, \end{cases}$$

where $T > 0$ is the so-called cellular temperature of the system. This value of T can be manually chosen and affects the likelihood of energetically unfavorable alterations getting accepted, this probability increases with the value of T . Note that $\mathcal{P}(\Delta\mathcal{H})$ is a decreasing function of $\Delta\mathcal{H}$, which implies that the probability that a spin copy is accepted decreases as the difference in energy increases. For a $n \times m$ grid, this algorithm is performed $n \cdot m$ times at every Monte Carlo step. As a result, every grid site on average receives one potential spin copy at every time-step.

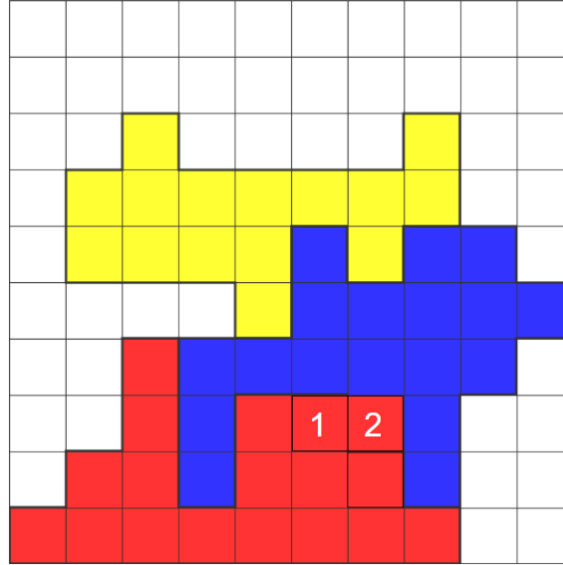


Figure 2.2: New configuration after spin copy of site 1 into site 2.

2.2 The Hamiltonian

In the previous subsection, we discussed the Hamiltonian, which represents the total energy of the system. We will now dive deeper into the specifics of this Hamiltonian. By doing this, it will become clear how it influences the behavior of the cells in such a way that they act most naturally. We define the Hamiltonian as a sum of five different terms:

$$\mathcal{H} = \mathcal{H}_A + \mathcal{H}_P + \mathcal{H}_L + \mathcal{H}_J + \mathcal{H}_M, \quad (2.1)$$

where the term \mathcal{H}_A is tied to the cell area, \mathcal{H}_P to the cell perimeter, \mathcal{H}_L to the cell length, \mathcal{H}_J to the adhesion between two different cells and the surrounding medium and \mathcal{H}_M is tied to directed cell motion. Before we specifically analyze each term, we define the neighborhood of \mathbf{x} . Let $\mathcal{N}(\mathbf{x})$ be the set of direct neighbors of grid site \mathbf{x} . We use a neighborhood of order two, which gives that $\mathcal{N}(\mathbf{x})$ has eight elements (when \mathbf{x} is not at the boundary).

Let us now begin with the area constraint \mathcal{H}_A . Recall that $\mathcal{P}(\Delta\mathcal{H})$ is a decreasing function of $\Delta\mathcal{H}$ such that adjustments that increase the total energy are less likely to be accepted. We want the cells in our model to stay roughly the same area throughout the entire simulation, we must therefore make sure that \mathcal{H}_A is large when the cell deviates from its original size. We consider the difference $a_\sigma - A_\sigma$, where a_σ is the total area and A_σ is the target area of all cells with spin value σ . We take the square of this difference, sum over all values of σ and multiply by $\lambda_{A,\sigma}$. This final term, known as the Lagrange multiplier, sets the strength of the area constraint for cells with spin value σ . Putting it all together we now have

$$\mathcal{H}_A = \sum_{\sigma \in S} \lambda_{A,\sigma} (a_\sigma - A_\sigma)^2. \quad (2.2)$$

In the same way, we want the cells in our model to keep roughly the same perimeter throughout the simulation, as the cell may otherwise still fluctuate a lot in shape. Additionally, we might also consider a restriction to the cell length by means of a length constraint. Both these constraints \mathcal{H}_P and \mathcal{H}_L are analogous to the area constraint and thus have the same form as visible in Equation (2.7). Constraint \mathcal{H}_P has strength $\lambda_{P,\sigma}$ and target P_σ and constraint \mathcal{H}_L has strength $\lambda_{L,\sigma}$ and target L_σ .

We can also consider an adhesion constraint \mathcal{H}_J . Some cells naturally tend to bind more easily to the medium or specific cells than others. For this reason, we want the total energy of the system to depend on which cells are in direct contact to specific other cells or the medium. To acquire this, we assign an adhesion energy $J(\tau_1, \tau_2)$ to every pair of cell types including the medium. Now for every grid site \mathbf{x} and for all its direct neighbors $\mathbf{x}' \in \mathcal{N}(\mathbf{x})$ we sum up the adhesion energy values only if \mathbf{x} and \mathbf{x}' belong to a different cell type. This can be done by introducing the complement of the Kronecker delta function $1 - \delta_{\sigma_{\mathbf{x}}, \sigma_{\mathbf{x}'}}$ which equals 1 if and only if $\sigma_{\mathbf{x}} \neq \sigma_{\mathbf{x}'}$ when \mathbf{x} and \mathbf{x}' are both on the boundary of two different cells. We can now write

the adhesion constraint as:

$$\mathcal{H}_J = \sum_{\mathbf{x}} \sum_{\mathbf{x}' \in \mathcal{N}(\mathbf{x})} J(\tau(\sigma_{\mathbf{x}}), \tau(\sigma_{\mathbf{x}'})) \cdot (1 - \delta_{\sigma_{\mathbf{x}}, \sigma_{\mathbf{x}'}}). \quad (2.3)$$

Observe Figure 2.3 to get an idea of the effect of this adhesion energy J . Here we see two cells with four different combinations of adhesion energies. J_{aa} represents the adhesion energy between the two cells and J_{am} represents the adhesion energy between the cells and the surrounding medium. We can observe that the cells drift apart when $J_{aa} > J_{am}$ and that the cells stick closely together when $J_{aa} < J_{am}$. In general, the higher the value of J_{aa} and the lower the value of J_{am} , the less cells stick to each other.

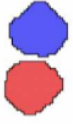
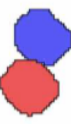
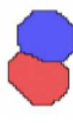
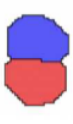
Adhesion Energies	$J_{aa}=10$ $J_{am}=4$	$J_{aa}=4$ $J_{am}=2$	$J_{aa}=2$ $J_{am}=4$	$J_{aa}=4$ $J_{am}=10$
Results				

Figure 2.3: Cell adhesion behavior for different combinations of J_{aa} and J_{am} [9]

Finally we include the term \mathcal{H}_M in the Hamiltonian, which models directed cell motion. In our model we consider a sheet of cells where the cells collectively migrate towards the right edge. The driving force of this migration is caused by cell polarization [10]. This polarization is initiated at the front edge of the sheet of cells and slowly expands backwards, see Figure 2.4 for an illustration of this initial polarization.

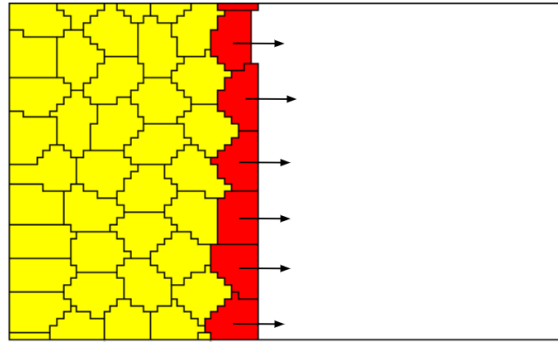


Figure 2.4: Illustration of initial polarization, the red cells are polarized but the yellow cells are not.

In our model, the cell polarization is represented by the vector \vec{p}_σ . Using this polarization vector, the driving force vector \vec{F}_σ is calculated by means of the Hill

function and the parameters for the maximum force F_{\max} , the half-saturation rate α and the hill coefficient n .

$$\vec{F}_\sigma = F_{\max} \frac{\vec{p}_\sigma}{|\vec{p}_\sigma|} \frac{|\vec{p}_\sigma|^n}{|\vec{p}_\sigma|^n + \alpha^n} \quad (2.4)$$

Additionally, the cell polarization vector \vec{p}_σ changes over time via the following differential equation. Here β is the depolarization rate and φ is the polarization rate.

$$\frac{d\vec{p}_\sigma}{dt} = -\beta\vec{p}_\sigma(t) + \varphi\vec{v}_\sigma(t) \quad (2.5)$$

This equation assumes that the cell polarization increases proportional to the cell velocity $\vec{v}_\sigma(t)$ with rate φ and decreases proportional to its own polarization with rate β . Using the driving force vector of Equation (2.4) we define the Hamiltonian as the negative of the dot product of the force vector and the vector \vec{r}_σ between the cell's current center of mass and the proposed new center of mass. This makes sure that the cell is biased to move in the direction of the polarization vector.

$$\mathcal{H}_M = - \sum_{\sigma \in S} \vec{F}_\sigma \cdot \vec{r}_\sigma \quad (2.6)$$

When we combine the formulas for the Hamiltonian of the individual constraints, we acquire the following expression for the final Hamiltonian:

$$\begin{aligned} \mathcal{H} = & \sum_{\sigma \in S} \lambda_{A,\sigma} (a_\sigma - A_\sigma)^2 + \lambda_{P,\sigma} (p_\sigma - P_\sigma)^2 + \lambda_{L,\sigma} (l_\sigma - L_\sigma)^2 + \\ & \sum_{\mathbf{x}} \sum_{\mathbf{x}' \in \mathcal{N}(\mathbf{x})} J(\tau(\sigma_{\mathbf{x}}), \tau(\sigma_{\mathbf{x}'})) \cdot (1 - \delta_{\sigma_{\mathbf{x}}, \sigma_{\mathbf{x}'}}) - \sum_{\sigma \in S} \vec{F}_\sigma \cdot \vec{r}_\sigma. \end{aligned} \quad (2.7)$$

2.3 Model Assumptions

In mathematical modeling we must always make some simplifications and assumptions. This is done to decrease the complexity and increase the efficiency of our model. The assumptions that are used in our model are listed below:

1. The fibroblasts and myofibroblasts exist in a two-dimensional plane.
2. The cellular environment exists only of fibroblasts and myofibroblasts.
3. Cell proliferation and apoptosis (programmed death) do not occur.
4. The cell dynamics follow the rules of the CPM.
5. The chemical substances considered in the study are: unbound LLC, bound LLC and active TGF- β .
6. The only driving force behind cell migration is polarization, which follows the dynamics of Equations (2.4) and (2.5).
7. There is a continuous supply of unbound LLC in the wound.

3 The Reaction-Diffusion Model

In this section we will state and analyze a reaction-diffusion model representing TGF- β concentrations in different forms. We will model active TGF- β (w), unbound LLC (u) and bound LLC (v) using a system of three coupled partial differential equations. The model is an adjusted version of the model in [11]. We now only consider a system of three partial differential equations instead of four. In our model we do not model the concentration of available LLC receptors on the ECM using a differential equation. Instead we assume the total capacity is constant at B and implement a direct formula to model the available space. This decreases unnecessary complexity of the system of differential equations.

3.1 Model Description

Below we find the system of equations governing the concentration of the different forms of TGF- β , where $u(\mathbf{x}, t)$ represents the concentration unbound LLC, $v(\mathbf{x}, t)$ represents the bound LLC and finally $w(\mathbf{x}, t)$ represents the active TGF- β . See Figure 1.2 for an illustration of the different forms of TGF- β .

$$\begin{aligned}\frac{\partial u}{\partial t} &= p(\mathbf{x}) - \varepsilon_u u - ru \left(1 - \frac{v}{B}\right) + D_u \nabla^2 u \\ \frac{\partial v}{\partial t} &= ru \left(1 - \frac{v}{B}\right) - \gamma(\mathbf{x})v + D_v \nabla^2 v \\ \frac{\partial w}{\partial t} &= \gamma(\mathbf{x})v - \varepsilon_w w + D_w \nabla^2 w\end{aligned}\tag{3.1}$$

The decay of u and w is regulated by the parameters ε_u and ε_w respectively. The term $ru \left(1 - \frac{v}{B}\right)$ models the binding of the LLC to the ECM with total binding capacity B and coefficient r . We assume that all three different forms of TGF- β diffuse through the domain, this diffusion is modeled using the Laplace operator and diffusion rates D_u , D_v and D_w . As v represents the LLC that is bound to the ECM, the diffusion will be very small. Similarly, active TGF- β can diffuse more freely than unbound LLC because the molecular complex is smaller. We therefore assume $D_v \ll D_u \ll D_w$. Finally, the functions $p(\mathbf{x})$ and $\gamma(\mathbf{x})$ represent secretion of the unbound LLC by the wound and the release of active TGF- β respectively. We assume that the secretion of unbound LLC only occurs at the wound where $x > \hat{x}$. We also assume that the release of active TGF- β is greater near a myofibroblast than near a fibroblast, giving release rates $\tilde{\gamma}_1$ and $\tilde{\gamma}_2$ with $\tilde{\gamma}_1 < \tilde{\gamma}_2$. Following this reasoning, $p(\mathbf{x})$ and $\gamma(\mathbf{x})$ take on the following forms:

$$p(\mathbf{x}) = p_0 \cdot \mathbf{1}_{x > \hat{x}}, \quad \gamma(\mathbf{x}) = \begin{cases} \tilde{\gamma}_1 & \text{if } \tau_{\sigma(x)} = 1 \\ \tilde{\gamma}_2 & \text{if } \tau_{\sigma(x)} = 2 \end{cases}\tag{3.2}$$

Note that $\mathbf{x} = (x, y)$. This means that $p(\mathbf{x})$ only depends on the x -coordinate, but $\gamma(\mathbf{x})$ depends on both the x -coordinate and the y -coordinate. Additionally, no flux boundary conditions are imposed on the left and the right boundary. Throughout this project, the initial values for u , v and w are set to zero. In Table 3.1, the

parameter values for System (3.1) are used in Section 4.3.

Table 3.1: *Parameter values for System (3.1) which describes the dynamics of the molecules.*

Parameter	Description	Value
ε_u	Decay rate of u	0.001
ε_w	Decay rate of w	0.001
r	Binding coefficient for u	0.01
B	Binding capacity of u	0.7
p_0	Secretion rate of u	0.05
$\tilde{\gamma}_1$	Release rate of fibroblasts	0.05
$\tilde{\gamma}_2$	Release rate of myofibroblasts	0.1
D_u	Diffusion coefficient of u	1
D_v	Diffusion coefficient of v	0.02
D_w	Diffusion coefficient of w	10

3.2 Turing Pattern Analysis

For certain reaction-diffusion systems in biology, it is possible to find that a pattern formation occurs. We will now look at the possibility that our system will express Turing pattern formation. This is a concept that is introduced by the mathematician Alan Turing in a 1952 paper called "The Chemical Basis of Morphogenesis" [12]. In this paper, Turing showed that under the right conditions a homogeneous steady state solution can become unstable, after which the system can display structured repeating patterns called Turing patterns. This kind of pattern formation is quite common in biology and is, among others, thought to be responsible for the formation of stripes on animal fur and human fingerprints. See Figure 3.1 for an example of Turing pattern formation.

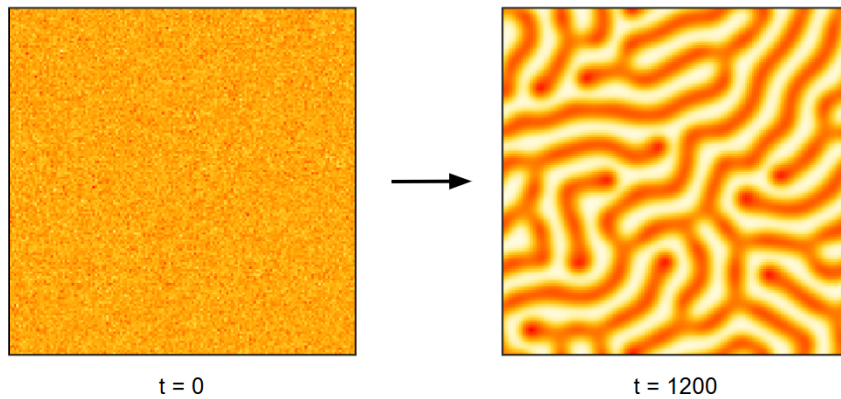


Figure 3.1: *Example of Turing pattern formation. Initial random distribution at $t = 0$ after which pattern formation is visible at $t = 1200$. High concentrations of the substance are colored red and low concentrations are colored white/yellow.*

In order to simplify the mathematical analysis, we will only consider one dimension

and we will make the following two assumptions:

$$p(x) = 0, \quad \gamma(x) = \tilde{\gamma}$$

This means that the secretion of the unbound LLC (u) by the wound is set to zero and that the release of active TGF- β (w) is assumed to be constant and independent of the position of the myofibroblasts.

Additionally we will write the system in the following way:

$$\frac{\partial u}{\partial t} = f(u, v, w) + D_u \frac{\partial^2 u}{\partial x^2} \quad (3.3)$$

$$\frac{\partial v}{\partial t} = g(u, v, w) + D_v \frac{\partial^2 v}{\partial x^2} \quad (3.4)$$

$$\frac{\partial w}{\partial t} = h(u, v, w) + D_w \frac{\partial^2 w}{\partial x^2} \quad (3.5)$$

Where the functions f, g and h are given by

$$f(u, v, w) = -\varepsilon_u u - ru \left(1 - \frac{v}{B}\right) \quad (3.6)$$

$$g(u, v, w) = -\tilde{\gamma}v + ru \left(1 - \frac{v}{B}\right) \quad (3.7)$$

$$h(u, v, w) = \tilde{\gamma}v - \varepsilon_w w \quad (3.8)$$

3.2.1 Homogeneous Steady State Solutions

In order to investigate the possibility of Turing-type pattern formation, we first need to find the homogeneous steady state solutions (HSS). For this reason, we set all derivatives to zero and solve the resulting three equations for u , v and w , so we solve:

$$f(u, v, w) = 0 \quad (3.9)$$

$$g(u, v, w) = 0 \quad (3.10)$$

$$h(u, v, w) = 0 \quad (3.11)$$

This system of equations turns out to have two solutions: one trivial and one non-trivial solution.

$$\mathbf{z}_0 = (u_0, v_0, w_0) = (0, 0, 0) \quad (3.12)$$

$$\mathbf{z}_1 = (u_1, v_1, w_1) = \left(-\frac{\tilde{\gamma}B(\varepsilon_u + r)}{r\varepsilon_u}, \frac{B(\varepsilon_u + r)}{r}, \frac{\tilde{\gamma}B(\varepsilon_u + r)}{r\varepsilon_w} \right) \quad (3.13)$$

For the second solution \mathbf{z}_1 we have that $u_1 < 0$. This would mean that the concentration of unbound LLC (u) is negative, which is not physically possible. For this reason, we will not further investigate \mathbf{z}_1 .

3.2.2 Stability of Homogeneous Steady State Solutions

One condition for Turing pattern formation is the stability of the HSS. We investigate the stability of solution \mathbf{z}_0 . We begin by defining the Jacobian matrix \mathbf{J} :

$$\mathbf{J} = \begin{bmatrix} \frac{\partial f}{\partial u} & \frac{\partial f}{\partial v} & \frac{\partial f}{\partial w} \\ \frac{\partial g}{\partial u} & \frac{\partial g}{\partial v} & \frac{\partial g}{\partial w} \\ \frac{\partial h}{\partial u} & \frac{\partial h}{\partial v} & \frac{\partial h}{\partial w} \end{bmatrix} = \begin{bmatrix} -\varepsilon_u - r \left(1 - \frac{v}{B}\right) & \frac{ru}{B} & 0 \\ r \left(1 - \frac{v}{B}\right) & -\tilde{\gamma} - \frac{ru}{B} & 0 \\ 0 & \tilde{\gamma} & -\varepsilon_w \end{bmatrix}. \quad (3.14)$$

When we then substitute \mathbf{z}_0 in the Jacobian matrix we find:

$$\mathbf{J}|_{\mathbf{z}_0} = \begin{bmatrix} -\varepsilon_u - r & 0 & 0 \\ r & -\tilde{\gamma} & 0 \\ 0 & \tilde{\gamma} & -\varepsilon_w \end{bmatrix} \quad (3.15)$$

Note that this is a (lower) triangular matrix, which implies that its eigenvalues are simply the diagonal elements. Hence, we have:

$$\lambda_1 = -\varepsilon_u - r, \quad \lambda_2 = -\tilde{\gamma}, \quad \lambda_3 = -\varepsilon_w \quad (3.16)$$

Note that all parameters are defined to be positive so we find that all three eigenvalues λ_1 , λ_2 and λ_3 are negative, which implies that equilibrium solution \mathbf{z}_0 is stable.

3.2.3 Non-Existence of Wave-number

We now investigate the possibility of Turing-type pattern formation following the methods of [13]. When pattern formation does occur, we can define its wave number q to be the number of pattern elements per unit length. It turns out that a necessary and sufficient condition for pattern formation is the instability of the HSS when we include diffusion in the Jacobian matrix in the following way:

$$\mathbf{J}|_{\mathbf{z}_0} - q^2 \mathbf{I} \cdot \begin{pmatrix} D_u \\ D_v \\ D_w \end{pmatrix} = \begin{bmatrix} -\varepsilon_u - r - D_u q^2 & 0 & 0 \\ r & -\gamma - D_v q^2 & 0 \\ 0 & \gamma & -\varepsilon_w - D_w q^2 \end{bmatrix}. \quad (3.17)$$

Note that the resulting matrix is again a triangular matrix, so the eigenvalues are the diagonal elements:

$$\lambda_1 = -\varepsilon_u - r - D_u q^2, \quad \lambda_2 = -\tilde{\gamma} - D_v q^2, \quad \lambda_3 = -\varepsilon_w - D_w q^2 \quad (3.18)$$

No q exists that makes any of the above eigenvalues non-negative, so the HSS \mathbf{z}_0 remains stable and no Turing-patterns can be formed.

3.3 Numerical Analysis

In this subsection, we will numerically analyze System (3.1) in one dimension. We do this to get an idea of the behavior of the system for two different functions $\gamma(\mathbf{x})$. For this analysis, the Runge-Kutta method with a timestep of 1 is used. First, we

assume $\gamma(\mathbf{x})$ is a constant and equal to 0.5. In Figure 3.2 we find a plot of u , v and w at four different time-steps.

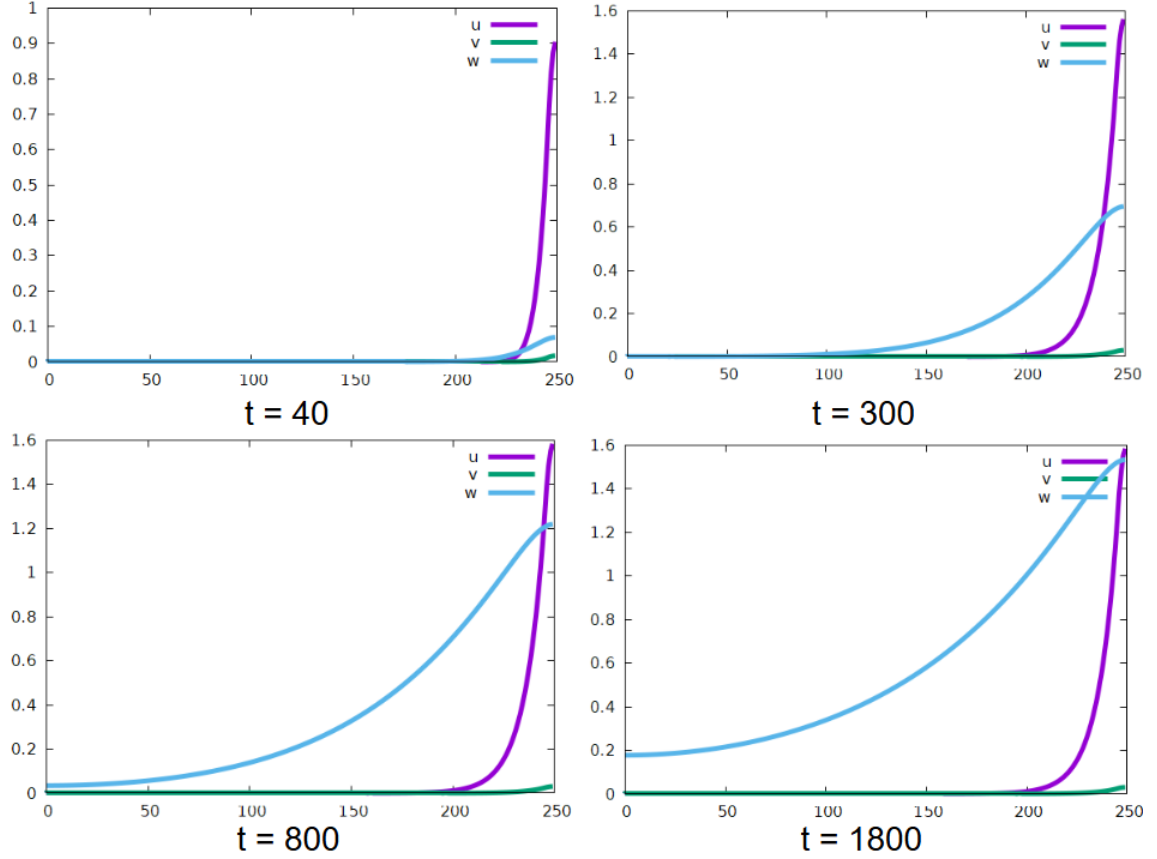


Figure 3.2: Plot of u , v and w with constant $\gamma(\mathbf{x})$ at time-steps 40, 300, 800 and 1800.

We see that u has high values close to the right boundary, this can be explained by the secretion of unbound LLC at the wound site. Interestingly, v remains very small throughout the whole simulation, it now only serves as a buffer for the transition of u into w . Lastly, w increases closer to the right boundary but keeps rising and retains somewhat of the same shape throughout the entire simulation. This simulation shows that u and v are quickly depleted in order for w to grow.

We now assume that we have a sheet of cells that has migrated to about $x = 200$. Throughout this sheet of cells we find myofibroblasts that linearly increase in number the closer they get to the front layer of cells at $x = 200$. We can adapt $\gamma(\mathbf{x})$ to model this distribution of myofibroblasts in the following way:

$$\gamma(\mathbf{x}) = \begin{cases} \frac{1}{200}x & \text{if } x \leq 200 \\ 0 & \text{if } x > 200 \end{cases} \quad (3.19)$$

Figure 3.3 shows the numerical simulation for this adjusted $\gamma(\mathbf{x})$. We can see that again u rises quickly and grows at the right boundary. Due to the form of $\gamma(\mathbf{x})$ we get that v is approximately zero for $x < 200$ and rises for $x > 200$. As the total binding capacity (B) is set to 0.7, we find that v approaches this limit for $x > 200$

where $\gamma(\mathbf{x})$ is equal to zero. Finally, w rises with a small peak at $x = 200$, but remains relatively flat due to its high diffusion coefficient. For large time-steps, u and v retain relatively the same value, but w steadily but slowly increases.

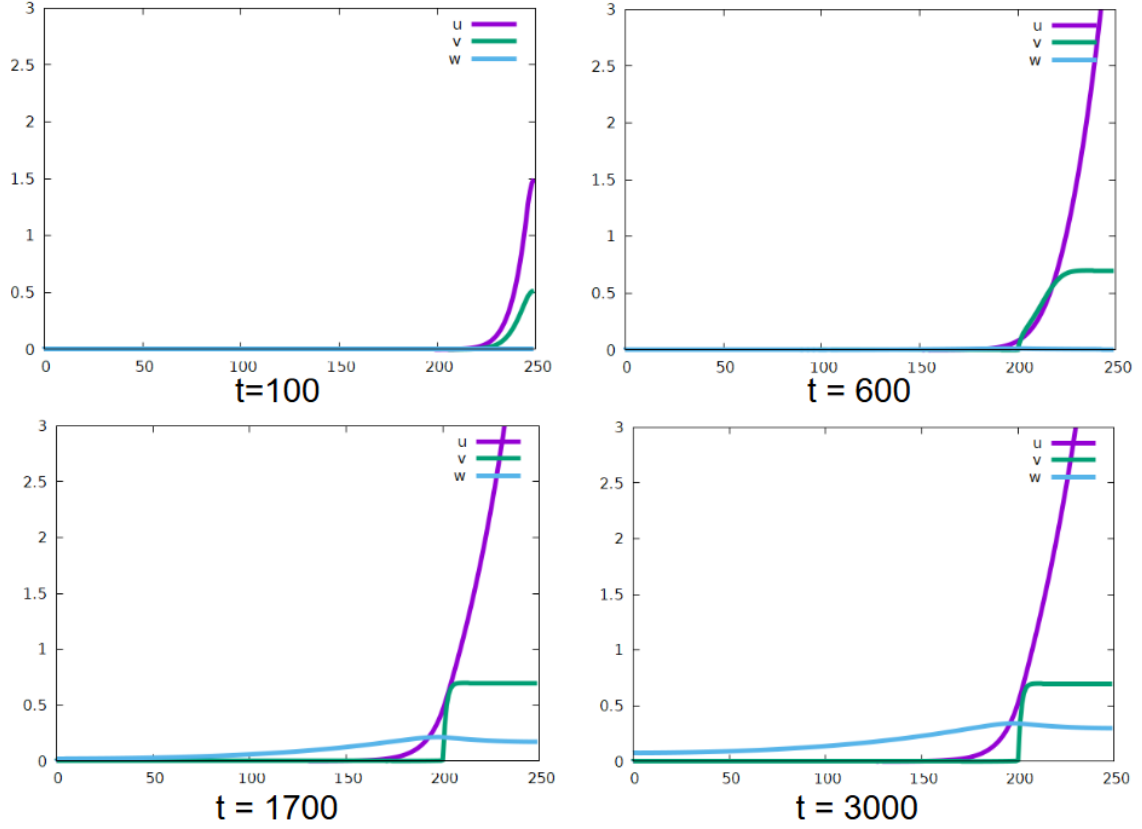


Figure 3.3: Plot of u , v and w with adjusted $\gamma(\mathbf{x})$ at time-steps 100, 600, 1700 and 3000.

4 Wound-Healing Assay Simulations

In this section, we will model the wound-healing assay in Morpheus by simulating the cell migration of fibroblasts and myofibroblasts. We will look at three different versions of the cell migration model. We start with the baseline model where only fibroblasts are present, which do not differentiate into myofibroblasts, as the reaction-diffusing system for TGF- β is not included. In this baseline model, we assume that fibroblasts have a circular shape. Next, specific length and surface constraints are included, giving the fibroblasts an elongated shape which is more biologically accurate. Here, we will also investigate the effect of cell shape on vertical cell movement. Finally, the reaction-diffusion system for TGF- β is included so that differentiation of fibroblasts into myofibroblasts is enabled. In this last model, additional length and surface constraints are imposed to model the star-like shape of myofibroblasts.

Table 4.1 lists the parameter values that are used for the simulations in the project, if there is no specification. Note that the parameters A_σ and P_σ do not have one set value, and they are varied throughout this section. We define t_0 to be the value of t at the moment that the polarization is initialized.

Table 4.1: Parameter values used in the CPM for the numerical simulations.

Parameter	Description	Value
T	Temperature	1
$\lambda_{A,\sigma}$	Area constraint strength	1
$\lambda_{P,\sigma}$	Perimeter constraint strength	1
$\lambda_{L,\sigma}$	Length constraint strength	1
A_σ	Target area	50
P_σ	Target perimeter	-
L_σ	Target length	-
J_{cc}	Adhesion energy between two cells	12
J_{cm}	Adhesion energy between cell and medium	$24 + 16 \cdot \mathbf{1}_{t \geq t_0}$
F_{\max}	Maximal polarization force from Equation (2.4)	1.5
n	Hill coefficient from Equation (2.4)	10
α	Half-saturation rate from Equation (2.4)	1
β	Depolarization rate from Equation (2.5)	0.003
φ	Polarization rate from Equation (2.5)	0.01

4.1 Baseline model

For the baseline model, we only consider the migration of fibroblasts without the involvement of TGF- β . This illustrates the migration behavior in its simplest form. The simulation is initialized by placing all cells in the leftmost quarter on a 250 by 150 grid, see Figure 4.1. Some fibroblasts are colored black in order to better track the migration of single cells.

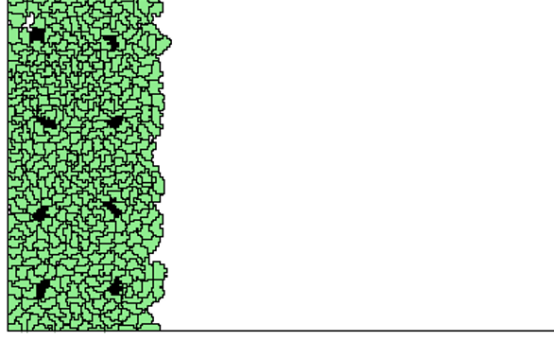


Figure 4.1: Configuration of the fibroblasts at $t = 25$.

The number of cells created is such that they take up half of the grid when the cells reach their target area, which is set to 50. Once the cells cover about half of the space at $t = 900$, the cells at the front get polarized in the x -direction with initial polarization value $p_0 = 1$, see Figure 4.2.

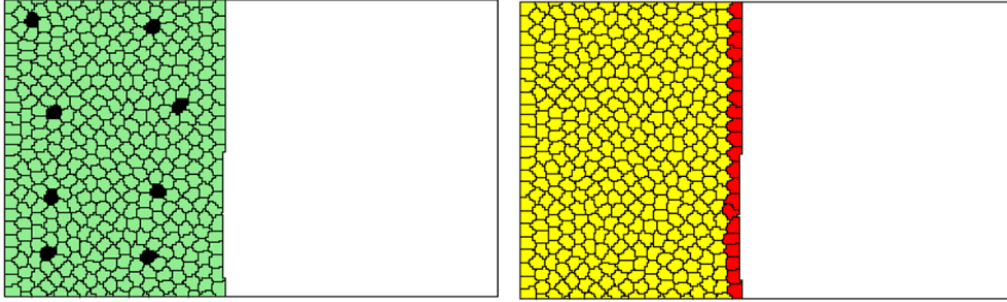


Figure 4.2: Cell configuration at $t = 900$ with fibroblasts colored green and black (left) and colored yellow (low) and red (high) showing polarization in the x -direction (right).

From this point on, the cells start to migrate to the right of the domain. The polarization of the front layer of cells now also starts to spread towards the cells further in the back following the dynamics of Equations (2.4) and (2.5). At the left boundary, new cells are added to fill up the empty space that would otherwise be created by the migration. See Figure 4.3 for the cell configuration and polarization in the time-steps following the initial polarization.

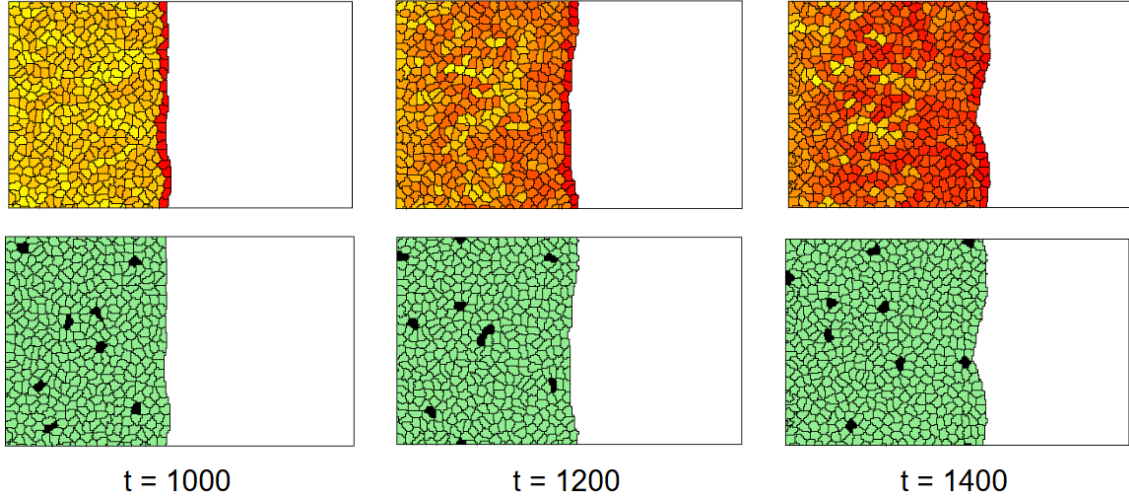


Figure 4.3: Cell configuration and polarization at $t = 1000$, $t = 1200$ and $t = 1400$.

At $t = 2350$ the cells have fully migrated to the right boundary and closed the gap. Just before this the polarization force is disabled to prevent the cells from accumulating at the right boundary, this is done by setting F_{max} to zero in Equation (2.4). See Figure 4.4 for the cell configuration at $t = 2350$ and just before the cells reach the right boundary at $t = 2225$.

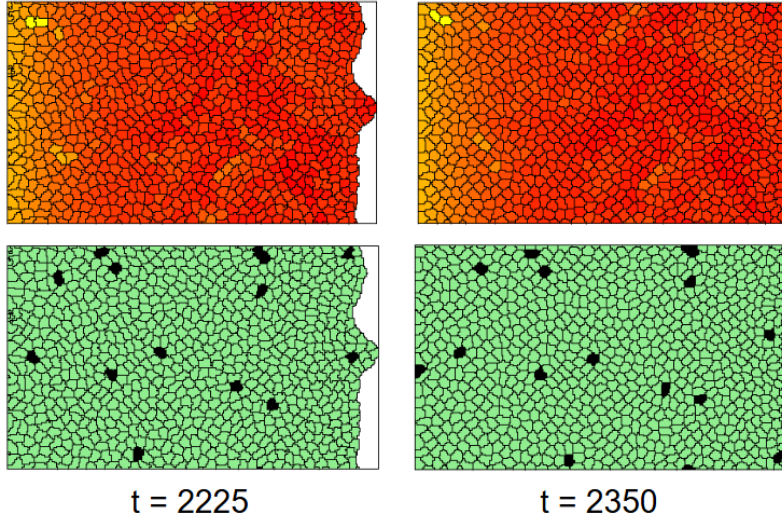


Figure 4.4: Cell configuration and polarization at $t = 2350$ and just before the cells reach the right boundary at $t = 2225$.

4.2 Baseline Model with Additional Shape Constraints

We will now look at the extended model with added length and perimeter constraints for the fibroblast cells. The target length and perimeter are set to 20 and 45 respectively and the target area is kept at 50. These constraints are meant to give the fibroblasts an elongated shape, which is more realistic. All other settings are similar to those of the baseline model of Subsection 4.1. See Figure 4.5 for the cell configuration and settings at $t = 900$ when the polarization is initialized.

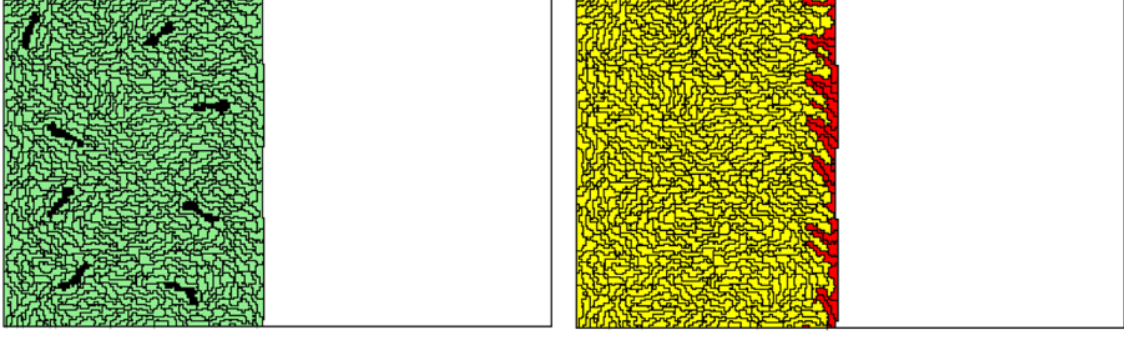


Figure 4.5: Cell configuration at $t = 900$ with fibroblasts again colored green and black (left) and colored yellow (low) and red (high) showing polarization in the x -direction (right).

Note that it might appear that there are more cells than in the baseline model, but this is not actually the case. We see that the fibroblasts do indeed have a more elongated shape. See Figure 4.6 for additional time-steps of this simulation.

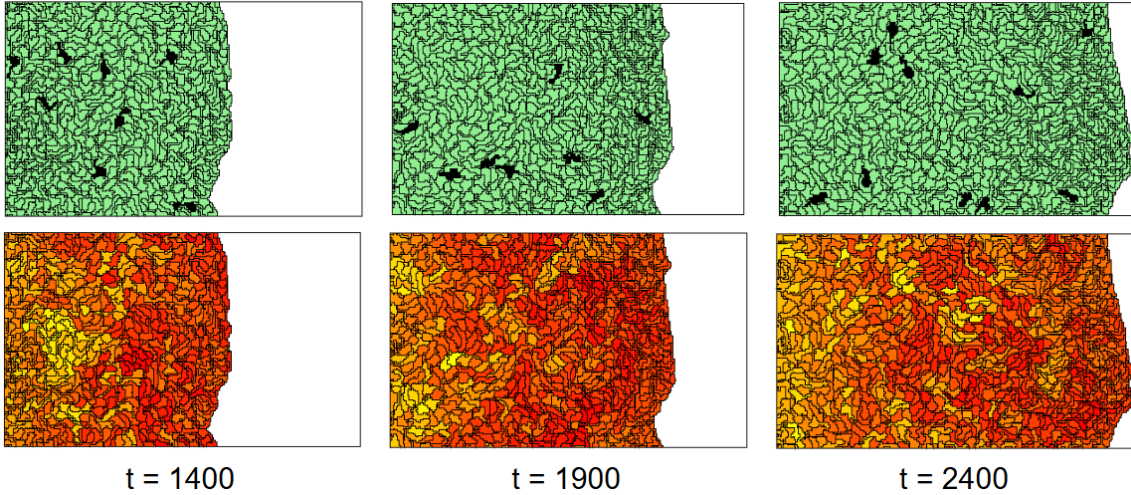


Figure 4.6: Cell configuration and polarization at $t = 1400$, $t = 1900$ and $t = 2400$.

We see that the fibroblast cells take on a slightly wider shape after the polarization is initialized than before. This is most likely due to the polarization forces pulling on the cells. Another interesting observation is the fact that the cells move a lot in the vertical direction. As the top and bottom of the domain have periodic boundary conditions, cells can easily "loop" from the top to the bottom or vice versa. In this model, it is not uncommon to see cells make one or two full rotations in this way. This behavior is not present in the baseline model, where the cells take on a more circular shape. A question then arises: is the vertical cell movement directly caused by the increased cell length? We will further investigate this question in the following subsection.

In the previous simulation, the edge of the cell layer remains relatively straight as the cells are migrating towards the right boundary. However, this is not the case for every simulation. In some cases, we see that one or multiple "fingers" of cells

extend from the edge and move towards the right boundary. This phenomenon is called "fingering". This can be caused by one of two things (or both). The first possible cause is that the front layer of cells is unequally distributed when the initial polarization occurs, at $t = 900$. Any cell present at the leading edge gets polarized at $t = 900$ when it is in contact with the medium, even when this contact is only very small. Because of this, the density of polarized cells can differ along the edge, see the circled area in Figure 4.7. The second possible cause of "fingering" is the adhesion energy settings (see Equation (2.3)). When the adhesion energy between cells and the medium is increased, the Hamiltonian also rises more rapidly when the length of the leading edge increases. This discourages the "fingering" behavior. See Figure 4.7 for an illustration of the "fingering" effect.

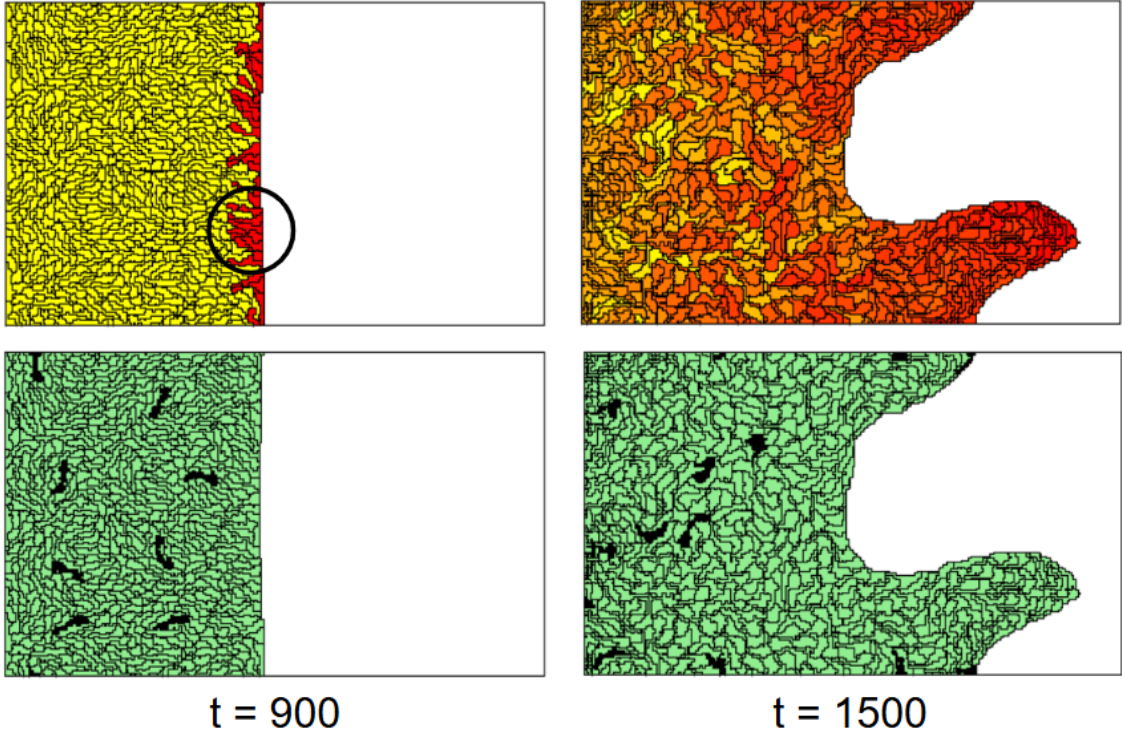


Figure 4.7: Illustration of "fingering" phenomenon. In the circled area, we see a cluster of polarized cells.

4.2.1 The Effect of Cell Length on Vertical Movement

In the previous subsection, we saw that vertical cell movement increased when we added length and perimeter constraints to the baseline model. Here, we increased the cell target perimeter from 25 to 45 and the cell target length from 8 to 20. This was done in order to change the cell shape from circular to elongated. We will now investigate the effects of these constraints by quantifying the vertical cell movement and comparing it to different target length and perimeter settings.

We represent the i 'th cell as c_i with $i \in \{1, 2, 3, \dots, n\}$ and n is the amount of cells in the simulation. The total vertical cell movement can be quantified using the velocity of every cell, this can be tracked within Morpheus. Now, for every timestep between

t_0 and t_1 of each cell c_i , the absolute value of the vertical component of the cell velocity vector $\vec{v}_{i,t}$ is summed up. We define this total value as Y_i and it is given by the formula:

$$Y_i = \sum_{t=t_0}^{t_1} |b_{i,t}|, \quad \text{with } \vec{v}_{i,t} = \begin{pmatrix} a_{i,t} \\ b_{i,t} \end{pmatrix}. \quad (4.1)$$

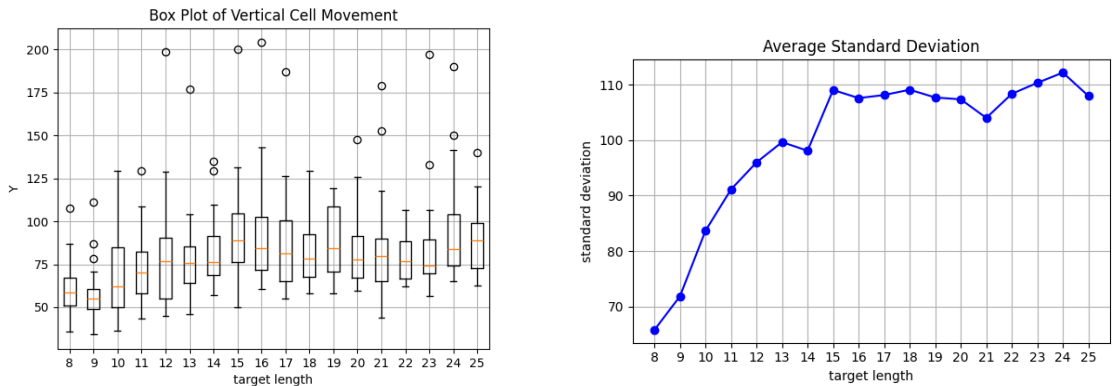
We will use $t_0 = 900$, which is when the polarization is initialized. The value of t_1 is equal to the moment when the average x -coordinate of all cells combined exceeds 115. This way we make sure that the final measurement is taken when the migration is nearly at its end, as in some simulations the cells migrate slightly faster than in other simulations. We then take the average value over every cell, which is given by:

$$\bar{Y} = \frac{1}{n} \sum_{i=1}^n Y_i. \quad (4.2)$$

We will use this as a representation of the total vertical cell movement. It can also be useful to know whether all cells display the same vertical movement and move as a collective or whether the vertical movement differs a lot from cell to cell. We therefore also calculate the standard deviation:

$$S_Y = \sqrt{\frac{\sum_{i=1}^n (Y_i - \bar{Y})^2}{n - 1}}. \quad (4.3)$$

We run the baseline model with varying cell target length and perimeter. The target length is varied from 8 to 25 with increments of 1, the target perimeter increases linearly to the target length following the formula: $25 + \frac{20(\text{target length}-8)}{12}$. For all eighteen length and perimeter combinations, a total of 20 simulations are run in order to mitigate the effects of randomness. Below we find two plots displaying the results of the simulations. In Figure 4.8a we see a box plot of \bar{Y} of the twenty simulations for each target length setting. In Figure 4.8b we find a line graph of the standard deviation (S_Y) for each target length averaged over all twenty simulations.



(a) Box plot of the vertical cell movement \bar{Y} for each target cell length. (b) Plot of standard deviation S_Y averaged over 20 simulations for each target cell length.

Figure 4.8: Box plot of \bar{Y} (left) and line graph of S_Y (right).

When viewing Figure 4.8 we can make a few interesting observations:

1. Between a target length of 8 and 15, it seems that \bar{Y} and S_Y are both increasing functions of the target cell length.
2. Between a target length of 15 and 25, \bar{Y} first decreases slightly and then increases slightly with an increasing target cell length. Around target length 15 and 25, \bar{Y} is generally the greatest.
3. Between a target length of 15 and 25, the standard deviation S_Y remains approximately constant but high. This is an indication of a lot of variation in the vertical movement between the different cells.
4. At target length 12 and beyond, there are more outliers for the value of \bar{Y} .

To investigate whether there is a significant difference in the values of \bar{Y} for different target length settings, for this we use a two-sample t-test. In Table 4.2 we see the p-values related to the comparison between the set of \bar{Y} values for target length 8 and 15 compared to every other target length. We take 0.05 as the significance level and observe that there is a significant difference in \bar{Y} between cell target length 8 and all other target length settings after 11. This means that there is a significant difference in \bar{Y} between the baseline model of Section 4.1 and the extended model of Section 4.3. Finally, there is no significant difference between cell target length 15 and all other target length settings after 15, this means that the above observation (2) is ungrounded.

4.3 Proof of Concept Model with Differentiation

In this final part, we implement the system of partial differential equations into the baseline model with added length and perimeter constraints. Additionally, when the fibroblasts encounter a sufficiently high concentration of active TGF- β , they can differentiate into myofibroblasts. The concentration threshold for differentiation is set to 0.1, after which at every ten time-steps differentiation can occur with a small probability (about 0.03). In order to model the star-like shape of myofibroblasts, the target area, length and perimeter are set to 50, 4 and 45 respectively. Due to the increased complexity of the simulations, we now only consider a grid of 100 by 60. Running this model on a grid of 250 by 150 takes too much time, the computations for the diffusion of the active TGF- β require a lot of computing power. Additionally, the cells are now spawned in the leftmost half of the domain and the polarization is initialized at $t = 300$. Below, Figure 4.9 displays the results of this model at time-step 300, 550, 800 and 1000, respectively. At each time step, there are four subfigures: the upper left displays a plot of the cell configuration and of the concentration of active TGF- β , the other three plots display the concentration of unbound LLC (u), bound LLC (v) and again active TGF- β (w). Note that this serves only as a proof of concept, many of the parameter values and simulation settings are estimated by trial and error or chosen to be convenient. Due to the time constraint of this project, we will also not perform any analyses on this extended model.

Table 4.2: Two-sample t -test performed on set of twenty \bar{Y} values for different cell length targets. The p -value indicates whether there is statistically significant difference in vertical displacement between the predefined target length (8 and 15, respectively) and other choices of target length.

Target Length (L_σ)	p-value ($L_\sigma = 8$)	p-value ($L_\sigma = 15$)
8	-	< 0.01
9	0.51	< 0.01
10	0.37	< 0.01
11	0.11	0.02
12	0.03	0.27
13	0.03	0.14
14	< 0.01	0.21
15	< 0.01	-
16	< 0.01	> 0.99
17	< 0.01	0.57
18	< 0.01	0.23
19	< 0.01	0.52
20	< 0.01	0.22
21	< 0.01	0.52
22	< 0.01	0.22
23	< 0.01	0.47
24	< 0.01	0.86
25	< 0.01	0.72

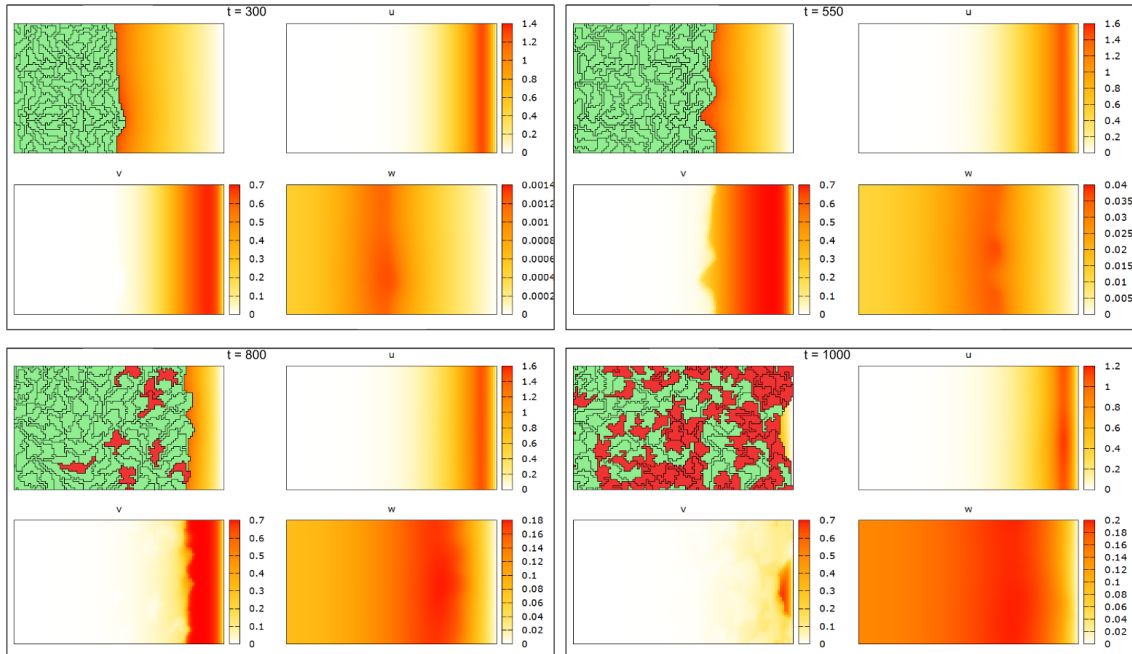


Figure 4.9: Four plots for each time-step 300, 550, 800 and 1000 of the extended model. The upper left displays the cell configuration and of the concentration of active TGF- β , the other three display the concentration of unbound LLC (u), bound LLC (v) and again active TGF- β (w).

5 Conclusion and Discussion

In this project, we investigated collective cell migration during wound healing. We presented a reaction-diffusion model consisting of three coupled partial differential equations for the different forms of the molecule TGF- β . After analyzing this system for the possibility of Turing-pattern formation, it became clear there are two homogeneous steady states, of which one is the trivial solution. It turns out that the non-trivial steady state is physically impossible and the trivial solution is stable but does not allow for Turing-patterns to form. We also numerically analyzed the reaction-diffusion system in one dimension to investigate its behavior for two different functions of the active TGF- β release term. From this analysis, it became clear that u and v deplete relatively quickly and exist mostly at the right of the domain. As a result, w steadily grows and because of its high diffusion coefficient, is well distributed throughout the entire domain.

We used the Cellular Potts Model and the software package Morpheus to simulate cell migration in a wound-healing assay context. A polarity-based approach was used for the driving force behind this migration. First, we created the baseline model with only fibroblasts showing the concept of the wound healing assay, here we assumed all cells are of a circular shape. The baseline model was extended by implementing additional length and perimeter constraints that model the elongated shape of fibroblasts. This extended baseline model showed that the cells move significantly more in the vertical direction, suggesting a link between cell shape and vertical movement. This phenomenon was investigated further by running multiple simulations for varying cell lengths. We calculated the total vertical movement averaged over every cell and performed a two-sample t-test. We found that there is a significant difference in vertical cell movement between the baseline model and the extended model. However, after increasing the cell length by approximately a factor of 2, further increasing the cell length does not significantly change the vertical cell movement. We also discovered that for high cell length settings, there is a lot of variation in vertical movement between the individual cells. Finally, we combined the reaction-diffusion with the extended baseline model. The result is a model serving as a proof of concept that demonstrates the differentiation of fibroblasts into myofibroblasts.

A large focus of this project was investigating the effect of the cell shape on the vertical cell movement. We found that, up to a certain point, increasing the cell length made the cells move more in the vertical direction. One question that remains is the cause of this vertical movement: is it an artifact of the CPM or does this phenomenon also occur in actual biological experiments? It is thought this is caused by the dynamics of how cells change their polarity based on their neighbors. Mathematical models that implement this polarity based migration often display a swirling pattern within the migration cells. Certain literature also shows that cells can display this swirling motion when cell migration is studied empirically [4, 14]. We found that, for high cell length settings, there is a lot of variation in vertical movement between the individual cells. This could indicate the presence of swirling

motions, where some cells are involved in a swirling pattern while other cells remain relatively stationary. We have not implemented a method to quantify the swirling motion, further research is necessary to investigate the relation between cell length and swirling.

The full model with fibroblast differentiation now also only serves as a proof of concept. It is also only run on a smaller grid due to its high computational cost. Due to time restrictions, no qualitative research is done on the full model. As a result, the effect of the differentiation of fibroblasts into myofibroblasts on cell migration remains to be investigated.

In this thesis, we used mathematical modeling to investigate cell migration, this automatically brings certain challenges with it. As a start, a lot of the reaction-diffusion equations and CPM parameters had to be estimated. This was mostly done by trial and error to acquire the desired behavior. A lot of parameters do not translate well into reality or are simply unknown. This estimation of parameters lowers the overall level of realism of the simulations. For the Turing analysis, we also had to assume that the unbound LLC secretion rate p_0 is equal to zero and the release function $\gamma(\mathbf{x})$ is constant. However, this is not actually the case. By changing these assumptions and adding other reaction terms, it might be possible to obtain more promising results when applying a different analysis method. A linear perturbation analysis can be performed to discover other patterns or wave analysis to find wave-like solutions. Lastly, our model is also necessarily a simplification of reality and some aspects are not included, for example cell proliferation and apoptosis as well as a more diverse chemical and cellular environment.

As the next step in this project, we could expand the full model with cell differentiation to the original grid size. Using this model, a qualitative analysis can be performed to investigate the effectiveness of the migration when varying certain parameters. Possible options include assigning fibroblasts and myofibroblasts a different maximum polarization force and changing the condition for which cell differentiation occurs. With this full model, it can be discovered what the effects are of the integration of the reaction-diffusion system as well as cell differentiation. Another possible improvement to the project is linking certain parameter values to empirical data. Many of these parameters do not translate well into reality, but some, such as the diffusion coefficients, can still be roughly estimated.

References

- [1] Yifan Tai, Emma L. Woods, Jordanna Dally, Deling Kong, Robert Steadman, Ryan Moseley, and Adam C. Midgley. Myofibroblasts: Function, formation, and scope of molecular therapies for skin fibrosis. *Biomolecules*, 11(8), 2021.
- [2] David John Leaper Stuart Enoch. Basic science of wound healing. *Surgery (Oxford)*, Feb 2008.
- [3] AE Postlethwaite, J Keski-Oja, HL Moses, and AH Kang. Stimulation of the chemotactic migration of human fibroblasts by transforming growth factor beta. *The Journal of experimental medicine*, 165(1):251–256, 1987.
- [4] Hamid Khataee, Andras Czirok, and Zoltan Neufeld. Multiscale modelling of motility wave propagation in cell migration. *Scientific Reports*, 10(1):8128, 2020.
- [5] Brigitte Li Olivier Cardoso Benoît Ladoux Hélène Delanoë-Ayari François Graner Sham Tlili, Estelle Gauquelin. Collective cell migration without proliferation: density determines cell velocity and wave velocity. *Royal Society Open Science*, 5(5):172421, May 2018.
- [6] Dietmar Oelz, Hamid Khataee, Andras Czirok, and Zoltan Neufeld. Polarization wave at the onset of collective cell migration. *Phys. Rev. E*, 100:032403, Sep 2019.
- [7] F Gabbiani G Gabbiani A Desmoulière, A Geinoz. Transforming growth factor-beta 1 induces alpha-smooth muscle actin expression in granulation tissue myofibroblasts and in quiescent and growing cultured fibroblasts. *The Journal of cell biology*, Jul 1993.
- [8] Jörn Starrauß, Walter De Back, Lutz Brusch, and Andreas Deutsch. Morpheus: a user-friendly modeling environment for multiscale and multicellular systems biology. *Bioinformatics*, 30(9):1331–1332, 2014.
- [9] Leah Edelstein-Keshet. *Mathematical Models in Biology*. SIAM, SIAM, 12 1987.
- [10] Zoltan Neufeld Hamid Khataee, Andras Czirok. Multiscale modelling of motility wave propagation in cell migration. *Scientific Reports*, 10(1), May 2020.
- [11] Mathé Zeegers. *Cellular Potts modelling of branching morphogenesis by chemical inhibition and mechanochemical feedback*. PhD thesis, 2017.
- [12] Alan Mathison Turing. The chemical basis of morphogenesis. 1952.
- [13] James D. Murray. *Mathematical Biology II*. Springer Science Business Media, Springer Science Business Media, 02 2011.
- [14] Kei Hashimoto, Kimiko Yamashita, Kanako Enoyoshi, Xavier Dahan, Tatsu Takeuchi, Hiroshi Kori, and Mari Gotoh. The effects of coating culture dishes with collagen on fibroblast cell shape and swirling pattern formation. *Journal of Biological Physics*, 46(4):351–369, Aug 2020.